Radiation Magnetohydrodynamic Simulations of Soft X-ray Emitting Regions in Active Galactic Nuclei

Taichi Igarashi[1] , Yoshiaki Kato[2], Hiroyuki R. Takahashi[3], Ken Ohsuga[4], Yosuke Matsumoto[1] and Ryoji Matsumoto[1]

[1]Chiba University, email: igarashi.taichi@chiba-u.jp

[2]RIKEN

[3]Komazawa University

[4]University of Tsukuba

Abstract. We present the results of global three-dimensional radiation magnetohydrodynamic simulations of the formation of soft X-ray emitting regions in active galactic nuclei by applying a radiation magnetohydrodynamic code based on the M1-closure scheme. The effect of Compton cooling is taken into account. When the surface density of the accretion flow exceeds the upper limit of the radiatively inefficient accretion flow (RIAF), the optically thin, hot accretion flow near the black hole co-exists with the soft X-ray emitting, warm ($T = 10^6 - 10^7$ K) Comptonized region around $r = 20 - 40r_{\rm s}$, where $r_{\rm s}$ is the Schwarzschild radius. Numerical results indicate that when the accretion rate approaches the Eddington accretion rate, the warm Comptonized region stays in optically thin for effective optical depth, Thomson thick, and radiation pressure dominant state. This region is found to oscillate between a geometrically thin, cool state and a geometrically thick state inflated by radiation pressure. The time variability of the accretion flow is consistent with that of the narrow-line Seyfert 1 galaxies.

Keywords. (magnetohydrodynamics:) MHD, radiative transfer, galaxies: active

---

1. Introduction

Soft X-ray excess is observed in luminous active galactic nuclei (AGN) such as Seyfert 1 galaxies. Since the temperature of the optically thick, standard disk around a supermassive black hole is in the order of 10^5 K, the soft X-rays should be emitted from a region different from standard disks. Recently, the appearance and disappearance of a soft X-ray excess component have been observed in changing look AGN (CLAGN), in which broad emission lines and soft X-ray excess are observed when the luminosity exceeds 0.5% of the Eddington luminosity (e.g., Noda & Done 2018). This transition can be explained by the state transition from RIAF to a radiatively cooled accretion flow, which occurs when the accretion rate exceeds the upper limit for RIAF.

Recently, 1-hour quasi-periodic oscillations (QPOs) have been observed in narrow-line Seyfert 1 (NLS1) galaxy RE J1034+396. The QPOs are superimposed on lower frequency time variabilities (e.g., Chaudhury et al. 2018). NLS1s show more rapid time variabilities than Seyfert 1 galaxies because their black hole mass is smaller. The accretion rate in NLS1 can exceed the Eddington accretion rate. The QPOs in RE J1034+396 are similar to the high-frequency QPOs observed in galactic black hole candidates in which QPOs are observed when their luminosity approaches 10% of the Eddington luminosity. The

1 hour period around a $10^6 M_\odot$ black hole corresponds to 30 Hz for $10 M_\odot$ black hole, which is the same order as the 67 Hz QPO observed in a galactic microquasar GRS 1915+105 (e.g., Morgan et al. 1997).

In addition to the high-frequency QPOs, lower frequency heart-beat oscillations are observed in GRS 1915+105. Honma et al. (1991) carried out 1-dimensional simulations of radiation pressure dominant, thermally unstable disk. They showed that limit-cycle oscillations between a radiation pressure dominant slim disk and a gas pressure dominant disk take place. Ohsuga (2006) reproduced heart-beat X-ray luminosity variations observed in GRS 1915+105 by 2-dimensional global radiation hydrodynamic simulations.

In the following, we present the results of global three-dimensional radiation magnetohydrodynamic simulations of accretion flows onto a supermassive black hole when the accretion rate approaches the Eddington accretion rate.

2. Basic Equations and Numerical Setup

We solve the RMHD equations, consisting of resistive-magnetohydrodynamic equations coupled with the 0th and 1st moments of radiation transfer equations in cylindrical coordinates (r, φ, z). General relativistic effects are considered using the pseudo Newtonian potential $\phi_{\rm PN} = -GM_{\rm BH}/(R - r_{\rm s})$, where $M_{\rm BH} = 10^7 M_\odot$ is the black hole mass, $R (= \sqrt{r^2 + z^2})$ is the distance from the black hole, $r_{\rm s} (= 2GM_{\rm BH}/c^2 = 3 \times 10^{12}$ cm) is the Schwarzschild radius, and G is the gravitational constant. We normalized physical quantities by the Schwarzschild radius $r_{\rm s}$, speed of light $c = 3 \times 10^{10}$ cm/s, and $t_0 = r_{\rm s}/c = 100$ s. The mass accretion rate is normalized by the Eddington mass accretion rate $\dot{M}_{\rm Edd} = L_{\rm Edd}/c^2$, where $L_{\rm Edd}$ is the Eddington luminosity.

The basic equations are expressed as follows:

$$\frac{\partial \rho}{\partial t} + \nabla \cdot (\rho \mathbf{v}) = 0, \tag{2.1}$$

$$\frac{\partial \rho \mathbf{v}}{\partial t} + \nabla \cdot (\rho \mathbf{v}\mathbf{v} + p_{\rm t}\mathbf{I} - \mathbf{B}\mathbf{B}) = -\rho \nabla \phi_{\rm PN} - \mathbf{S}, \tag{2.2}$$

$$\frac{\partial E_{\rm t}}{\partial t} + \nabla \cdot [(E_{\rm t} + p_{\rm t})\mathbf{v} - \mathbf{B}(\mathbf{v} \cdot \mathbf{B})] = -\nabla \cdot (\eta \mathbf{j} \times \mathbf{B}) - \rho \mathbf{v} \cdot \nabla \phi_{\rm PN} - cS_0, \tag{2.3}$$

$$\frac{\partial \mathbf{B}}{\partial t} + \nabla \cdot (\mathbf{v}\mathbf{B} - \mathbf{B}\mathbf{v} + \psi \mathbf{I}) = -\nabla \times (\eta \mathbf{j}), \tag{2.4}$$

$$\frac{\partial \psi}{\partial t} + c_{\rm h}^2 \nabla \cdot \mathbf{B} = -\frac{c_{\rm h}^2}{c_{\rm p}^2}\psi, \tag{2.5}$$

where ρ, $\mathbf{v}$, $\mathbf{B}$, and $\mathbf{j} = \nabla \times \mathbf{B}$ are the mass density, velocity, magnetic field, and current density, respectively. In addition, $p_{\rm t} = p_{\rm gas} + B^2/2$ is the total pressure, and $E_{\rm t} = \rho v^2/2 + p_{\rm gas}/(\gamma - 1) + B^2/2$ is the total energy, where $\gamma = 5/3$ is the specific heat ratio. We apply the so-called anomalous resistivity. The resistivity η becomes large when the drift velocity $v_{\rm d}$ exceeds the critical velocity $v_{\rm c}$ (Yokoyama & Shibata 1994). In equations (2.4) and (2.5), ψ is introduced so that the divergence-free magnetic field is maintained within minimal errors during time integration where $c_{\rm h}$ and $c_{\rm p}$ are constants. These equations are solved by the MHD code CANS+ (Matsumoto et al. 2019).

In equations (2.2) and (2.3), $\mathbf{S}$ and S_0 are the radiation momentum and the radiation energy source terms, respectively, and are derived by solving the frequency-integrated

0th and 1st moments of the radiation transfer equation expressed in the following form.

$$\frac{\partial E_{\rm r}}{\partial t} + \nabla \cdot \mathbf{F}_{\rm r}$$

$$= \rho \kappa_{\rm ff} c(a_{\rm r} T^4 - E_{\rm r}) + \rho(\kappa_{\rm ff} - \kappa_{\rm es})\frac{\mathbf{v}}{c} \cdot [\mathbf{F}_{\rm r} - (\mathbf{v} E_{\rm r} + \mathbf{v} \cdot \mathbf{P}_{\rm r})] + \rho \kappa_{\rm es} c E_{\rm r0} \frac{k_{\rm B}(T_{\rm e} - T_{\rm r})}{m_{\rm e} c^2} = cS_0,$$

$$\frac{1}{c^2}\frac{\partial \mathbf{F}_{\rm r}}{\partial t} + \nabla \cdot \mathbf{P}_{\rm r} = \rho \kappa_{\rm ff}\frac{\mathbf{v}}{c}(a_{\rm r} T^4 - E_{\rm r}) - \rho(\kappa_{\rm ff} + \kappa_{\rm es})\frac{1}{c}[\mathbf{F}_{\rm r} - (\mathbf{v} E_{\rm r} + \mathbf{v} \cdot \mathbf{P}_{\rm r})] = \mathbf{S}. \qquad (2.6)$$

The M1-closure is applied to relate the radiation stress tensor $\mathbf{P}_{\rm r}$ and radiation energy density $E_{\rm r}$ (see e.g., Lowrie et al. 1999). In Equations (2.6), $\kappa_{\rm ff} = 1.7 \times 10^{-25} m_{\rm p}^{-2}\rho T^{-7/2}$ cm^2/g is the free-free absorption opacity where $m_{\rm p}$ is the proton mass and $\kappa_{\rm es} = 0.4$ cm^2/g is the electron scattering opacity. The gas temperature, T, is related to the gas pressure and density by $p_{\rm gas} = \rho k_{\rm B} T/(\mu m_{\rm p})$, where $k_{\rm B}$, and $\mu = 0.5$ are the Boltzmann constant and mean molecular weight, respectively. $T_{\rm e} = \min(T, 10^9 \text{ K})$ and $T_{\rm r} = (E_{\rm r}/a_{\rm r})^{1/4}$ are the electron temperature and radiation temperature, respectively. For the initial conditions (Figure 1(a)), we set the rotational equilibrium torus embedding weak poloidal magnetic field (Kato et al. 2004). Initially, we calculate without radiation term until a quasi-steady state is attained. After that, we include radiation terms from $t = 1.1 \times 10^4 t_0$. We normalized density such that the accretion rate when the cooling term is included is close to the Eddington accretion rate. The over-dense region simulates the dense blob in the accretion flow (see Igarashi et al. 2020). The computational domain of our simulation is $0 \leq r < 2000r_{\rm s}$, $0 \leq \varphi < 2\pi$, and $|z| < 2000r_{\rm s}$; and the number of grid points is $(n_{\rm r}, n_\varphi, n_{\rm z}) = (464, 32, 464)$. Grid spacing is $0.1r_{\rm s}$ in the radial and vertical directions when $r < 20r_{\rm s}$ and $|z| < 5r_{\rm s}$ and increases outside the region. The absorbing boundary condition is imposed at $R = 2r_{\rm s}$, and the outer boundaries are free boundaries where waves can be transmitted.

3. Numerical Results of RMHD Simulations

The upper panel of Figure 1(b) shows the time-averaged distribution of azimuthally averaged density (top), temperature (middle), and the ratio of the radiation pressure to gas pressure + magnetic pressure in the poloidal plane after radiative cooling is switched on. Numerical results indicate that radiation pressure dominant torus is formed, oscillating in the vertical direction. At the early stage (left panels), the disk inflates due to radiation pressure because the radiation is trapped in the Thomson thick disk. The Thomson optical depth computed by

$$\tau_{\rm es} = \int_{\pm 100r_{\rm s}}^{0} \rho \kappa_{\rm es} dz. \qquad (3.1)$$

exceeds 10, so that radiation energy density quickly increases, and radiation pressure drives expansion of the disk both in vertical and radial direction. The gas temperature of the disk quickly decreases from 10^{10} K to 10^6 K in the radiation pressure supported torus. In the inner region $r < 15r_{\rm s}$, the gas temperature above or below the disk is around 10^8 K, and the Thomson optical depth exceeds 10 in the disk. However, the disk is optically thin for the effective optical depth ($\tau_{\rm eff} = \sqrt{\tau_{\rm es}(\tau_{\rm es} + \tau_{\rm ff})} < 0.01$). Thus we expect soft X-ray emission by thermal bremsstrahlung radiation and inverse Compton scattering from this region. The appearance of such a Thomson thick, warm Compton region is discussed by Kumar and Yuan (2021) in their search for steady transonic solutions for sub-Eddington accretion flows.

Rapid mass accretion takes place from the dense torus to the black hole. As the density of the disk decreases by expansion, Thomson optical depth decreases. This enables radiation to escape from the disk and enhances the radiative cooling rate. When the
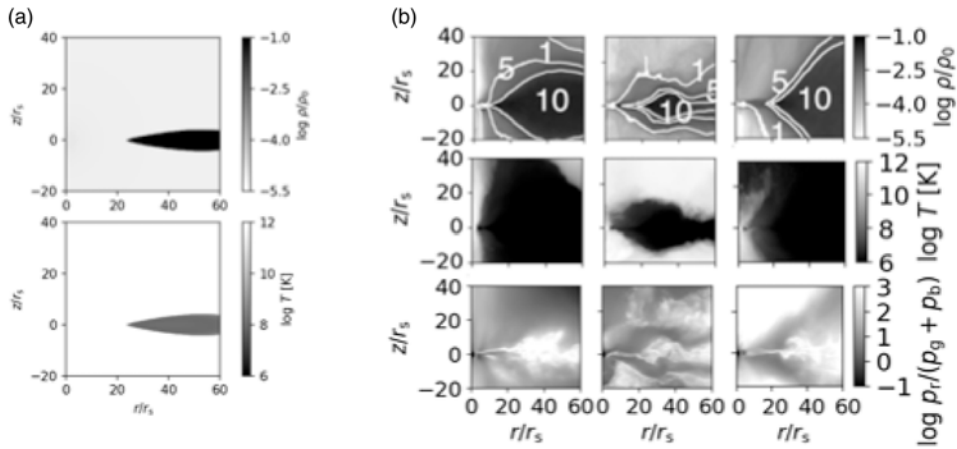
Figure 1. (a) Initial distribution of the gas density and gas temperature. (b) Azimuthally averaged gas density (top), gas temperature (middle), and the ratio of radiation pressure to gas pressure + magnetic pressure (bottom). The quantities are averaged over the time range $1.1 \times 10^4 t_0 < t < 1.175 \times 10^4 t_0$, $1.445 \times 10^4 t_0 < t < 1.475 \times 10^4 t_0$, and $1.675 \times 10^4 t_0 < t < 1.745 \times 10^4 t_0$, respectively from left to right. Contours in the upper panel show $\tau_{es} = 10, 5$, and 1. We include the radiation term from $1.1 \times 10^4 t_0$.

radiative cooling rate exceeds the heating rate of the disk, the disk shrinks in the vertical direction. Middle panels of figure 1(b) show that geometrically thin disk is formed in $r < 20 r_s$. The radiation pressure is comparable to the gas+magnetic pressure in this region. Subsequently, as the mass accumulates in the disk by accretion in $r > 20 r_s$, the radiation pressure of the disk becomes dominant.

Figure 2 shows the space-time plot of the radial velocity (left), surface density (middle), and radiation temperature (right), respectively. The surface density Σ is calculated by

$$\Sigma = \int_{z1}^{z2} \rho dz, \tag{3.2}$$

where $z1$ and $z2$ are the negative and positive z where the Thomson optical depth is $\tau_{es} = 1$. The left panel of figure 2 shows that the sign of the radial velocity outside $40 r_s$ reverses on a time scale of $\sim 3000 t_0$. The middle panel of figure 2 shows that dense torus is formed in $20 r_s < r < 60 r_s$ around $t = 1.1 \times 10^4 t_0$ and $t = 1.6 \times 10^4 t_0$. During the period $1.2 \times 10^4 t_0 < t < 1.5 \times 10^4 t_0$, the surface density of the disk decreases due to rapid mass accretion of the disk. In the region $r < 20 r_s$, low-density region is formed. In this region, radial oscillation of the disk is excited. The typical period of this oscillation is around $200 t_0$, which corresponds to several hours when the black hole mass is $10^7 M_\odot$. The oscillation frequency is around 50 Hz when the black hole mass is $10 M_\odot$.

4. Thermal Limit Cycle Oscillation

When the accretion rate onto a supermassive black hole is close to the Eddington accretion rate, the outer region around $r = 40 r_s$ oscillates between a geometrically thick disk and a radiatively efficient cool disk. This oscillation is similar to the thermal limit cycle oscillations in luminous accretion disks around a stellar-mass black hole. However, the normalized oscillation period ($\sim 3000 t_0$) is much shorter than the oscillations in a microquasar GRS 1915+105, whose period is $10^5 - 10^6 t_0$.

Figure 3 (a) shows the trajectory of the state transition of the disk in our RMHD simulation at $r = 40 r_s$. The horizontal axis shows surface density, and the vertical axis shows radiation pressure vertically integrated with the region where $\tau_{es} > 1$. The filled
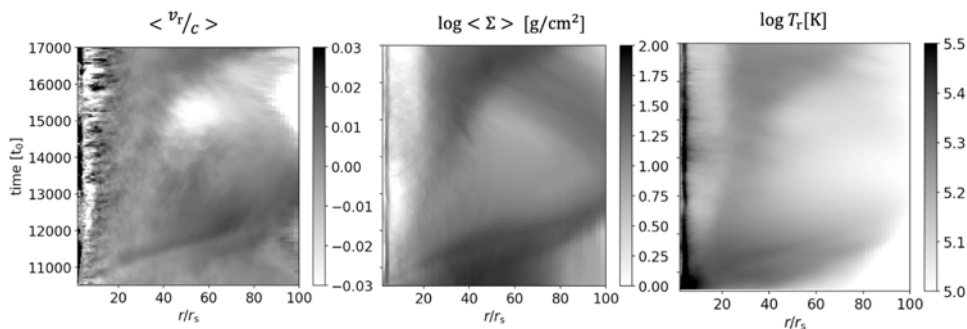
Figure 2. The space time diagram of the azimuthally averaged radial velocity, surface density, and radiation temperature, respectively.

circles plot the surface density and radiation pressure, and the greyscale shows time. As the radiation pressure increases, the accretion flow transits to a geometrically thick disk inflated by radiation pressure and stays in the state in $1.1 \times 10^4 t_0 < t < 1.3 \times 10^4 t_0$. During this stage, the surface density of the disk decreases by rapid accretion. Therefore, the radiation becomes easier to escape, and the radiative cooling rate increases. When the surface density becomes smaller than a threshold, the radiation pressure quickly decreases ($1.3 \times 10^4 t_0 < t < 1.4 \times 10^4 t_0$). Subsequently, surface density increases by mass accretion, and the next cycle starts around $t = 1.6 \times 10^4 t_0$.

Figure 3 (b) and (c) show the scatter plot of surface density and radiation flux F_z at $\tau_{es} = 1$, and the heating rate evaluated by $Q_{heat} = 3\dot{M}(1 - \sqrt{3 r_s/r})/(8\pi r^3)$, respectively. Heating balances with radiative cooling during the cool stage when the surface density increases by accretion ($1.3 \times 10^4 t_0 < t < 1.5 \times 10^4 t_0$). As the radiation pressure increases, heating exceeds cooling around $t = 1.5 \times 10^4 t_0$, and the disk expands again by radiation pressure.

The grey dots in figure 3(d) show the trajectory of the limit-cycle oscillation shown in the left panel. The vertical axis is the total pressure. Solid curves show the thermal equilibrium curves. The limit cycle oscillation is different from the oscillation between a gas pressure dominant disk and slim disk studied by Honma et al. (1991). The dotted curve shows the state where the radiation pressure equals the gas pressure. The dashdotted curve shows $\tau_{eff} = 1$, and the dashed curve shows $p_{rad} = p_{mag} + p_{gas}$. Dark dots show the trajectory of the lower accretion rate model reported in Igarashi et al. (2020).

Numerical results shown in figure 2 and 3 indicate that during the transition from a geometrically thick disk inflated by radiation pressure to a radiatively efficient cool disk, the disk stays in a radiation pressure dominant state. Therefore, a slight increase in surface density by mass accretion enables photons to be trapped again and enhances the radiation pressure. Thus, the time scale for the transition from the radiatively efficient cool state to the geometrically thick state becomes shorter than the viscous time scale. Azimuthal magnetic field enhanced by the vertical contraction of the disk prevents the disk collapsing to a gas pressure dominant, cool disk (see middle panel of figure 1 and the dashed curve in the figure 3(d)).

5. Summary

Results of three-dimensional global RMHD simulations of accretion flows when the accretion rate is comparable to the Eddington accretion rate are presented. Our numerical results indicate that limit cycle oscillations can be excited in Thomson thick, optically thin for effective optical depth but radiation pressure dominant disk. This mechanism
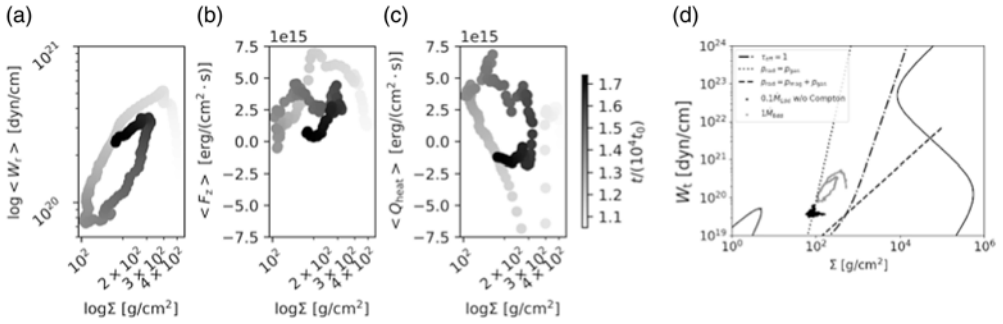
Figure 3. The scatter plot of the surface density and (a) vertically integrated radiation pressure, (b) radiative flux in $z-$direction at $\tau_{es} = 1$, and (c) heating rate $Q_{heat} = 3\dot{M}(1 - \sqrt{3r_s/r})/(8\pi r^3)$ at $r = 40r_s$. The radiation pressure is integrated with the region where $\tau_{es} > 1$. The greyscale of each point shows time. (d) The scatter plot of the surface density and vertically integrated total pressure at $r = 40r_s$. The total pressure is integrated in the region where $\tau_{es} > 1$. The dark dots show the results of Igarashi et al. (2020), and the grey dots show the results presented in this paper. The solid black curves show the thermal equilibrium curve. The dotted, dashed, and dash-dotted lines show the state where the gas pressure equals radiation pressure, magnetic pressure equals gas + radiation pressure, and effective optical depth $\tau_{eff} = 1$, respectively.

excites shorter time scale limit-cycle oscillation than those between gas pressure dominant disk and radiation pressure dominant slim disk. The appearance of this limit cycle oscillation is not clear in RMHD simulations by Jiang et al. (2019) probably because they started their simulation from a state nearly in thermal equilibrium.

The time scale of the oscillation in the outer region is $\sim 3000t_0$. Since the unit time $t_0 = 10$ sec when the black hole mass is $10^6 M_\odot$ the period of the thermal oscillation is 3×10^4 s ~ 8 hours. This time scale is close to the luminosity variations observed in NLS1 RE J1034+396 (Chaudhury et al. 2018). Numerical results indicate that higher frequency disk oscillation appears in the inner disk at $r < 20r_s$. The time scale of the oscillation is typically $\sim 200t_0 \sim 2000$ s ~ 0.5 hours. The oscillation frequency is close to the QPO observed in RE J1034+396.

References

Belloni, T. M., Bhattacharya, D., Caccese, P., et al. 2019, *MNRAS*, 489, 1037
Biang, W., & Zhao, Y. 2004, *MNRAS*, 352, 823
Chaudhury, K., Chitnis, V. R., Rao, A. R., et al. 2018, *MNRAS*, 478, 4830
Done, C., Davis, S. W., Jin, C., Blaes, O., & Ward, M. 2012, *MNRAS*, 420, 1848
Honma, F., Matsumoto, R., & Kato, S. 1991, *PASJ*, 43, 147
Igarashi, T., Kato, Y., Takahashi, H. R., et al. 2020, *ApJ*, 902, 103
Jiang, Y.-F., Stone, J. M., & Davis, S. W. 2019, *ApJ*, 880, 67
Kato, Y., Mineshige, S., & Shibata, K. 2004, *ApJ*, 605, 307
Kumar, R. & Yuan, Y. 2021, *ApJ*, 910, 9
Lowrie, R. B., Morel, J. E., & Hittinger, J. A. 1999, *ApJ*, 521, 423
Matsumoto, Y., Asahina, Y., Kudoh, Y., et al. 2019, *PASJ*, 71, 83
Morgan, E. H., Remillard, R. A., & Greiner, J. 1997, *ApJ*, 482, 993
Noda, H., & Done, C. 2018, *MNRAS*, 480, 3898
Ohsuga, K. 2006, *ApJ*, 640, 923
Takahashi, H. R., Ohsuga, K., Kawashima, T., & Sekiguchi, Y. 2016, *ApJ*, 826, 23
Yokoyama, T., & Shibata, K. 1994, *ApJ*, 436, L197